Eur. J. Mech. B - Fluids 20 (2001) 167–186

S0997-7546(00)01098-0/FLA

Selective withdrawal through a line sink of non-rotating and rotating stratified fluid in a reservoir of finite depth

Takeshi Kataoka *, Michihisa Tsutahara, Satoshi Mizutani

Graduate School of Science and Technology, Kobe University, Rokkodai, Nada, Kobe 657-8501, Japan

(Received 9 June 1999; revised 6 February 2000; accepted 18 May 2000)

Abstract – Selective withdrawal through a line sink of both non-rotating and rotating stratified fluid in a reservoir of finite depth is studied under an assumption that viscosity and diffusivity of the fluid are negligible. This flow is characterized by the two parameters: the Froude number F; and the ratio of the inertial frequency f to the buoyancy frequency N. Following the initiation of discharge from the sink, internal (or inertial) gravity wave modes propagate upstream. We first consider the case of $F \to 0$ to get linearized governing equations and seek a linear asymptotic solution for large t^* (where t^* is time after starting the discharge) which is uniformly valid in space. The obtained solution shows the propagation of the individual modes clearly and it is found that the amplitude of the modal front is kept constant with time t^* when $f = 0$, whereas it decreases as $t^{*-1/3}$ when $f > 0$. Next, numerical calculation is conducted to study the case of $F > 0$. Specifically, the validity of both our linear solution and the theory suggested by Clarke and Imberger in describing the mode propagation for $F > 0$ is explored. Investigations are also made of the flow patterns constructed by the passage of these modes. It is then found that the withdrawal-layer thickness shows strong time dependence whose period is about $6/f$. © 2001 Éditions scientifiques et médicales Elsevier SAS

selective withdrawal / line sink / columnar mode / stratified fluid / rotating stratified fluid

1. Introduction

When a stratified fluid is withdrawn from a sink, it is known that the withdrawn fluid comes from only a narrow horizontal layer adjacent to the sink level. This phenomenon, called selective withdrawal, has a wide application in both engineering and agricultural fields. Specifically, power plants draw their cooling water from a reservoir or sea stratified in temperature and therefore in density. In agricultural aspect, warmer water is needed in order to irrigate paddy fields and water of lowest salinity is desired if the withdrawal is done in an estuary stratified in salinity. The problem of selective withdrawal is also important as a water quality management technique in reservoirs [1]. In addition to these various practical applications, there is an interest in the nature of internal wave propagation in establishing the selective withdrawal. Therefore this problem has attracted many researchers [1–20]. To study this phenomenon, the line sink flow of a linearly stratified fluid in a reservoir of finite depth is the most frequently used model [1–18], since it gives fundamental understanding of this phenomenon and also it is easy to analyze.

It was Yih [2] who first studied this problem. He obtained the steady-state theoretical solution of selective withdrawal through a line sink of an inviscid, non-diffusive, non-rotating stratified fluid whose geometry is shown in *figure 1* (with $f = 0$). This flow is characterized by the Froude number defined by

$$F = Q/Nd^2, \tag{1}$$

* Correspondence and reprints.
E-mail address: kataoka@mech.kobe-u.ac.jp (T. Kataoka).

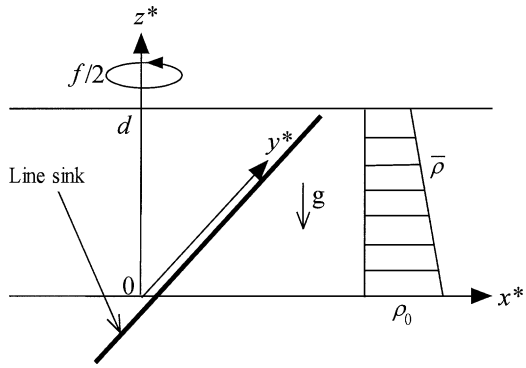

Figure 1. Geometry of the flow field.

where $2Q$, N, and d are the volumetric discharge per unit length of the line sink, the constant buoyancy frequency, and the depth of a reservoir, respectively. His solution shows the uniform withdrawal of fluid from all depths when $F > 1/\pi$. His solution, however, breaks down when $F < 1/\pi$, due to inadequacy of the uniform flow boundary condition far upstream, which means that the selective withdrawal occurs for $F < 1/\pi$. This fact was confirmed by experiments conducted later by Debler [3]. To supplement Yih's solution of the regime $F < 1/\pi$, Kao [5,7] introduced the so-called free streamline theory and obtained a steady-state solution of the line sink flow when the selective withdrawal occurs.

To understand the process of establishing the selective withdrawal, this flow must be treated as time-dependent problem starting from a quiescent state. It was Pao and Kao [9] who first clarified the evolution of selective withdrawal. They showed by linearized theory (which corresponds to an assumption that $F \to 0$) that internal waves of both frequency and horizontal wavenumber zero are continuously generated near the sink by keeping a constant volumetric discharge. These waves form an infinite set of modes whose vertical structures are expressed by the trigonometric function satisfying both the upper and the lower boundary conditions, and propagate horizontally upstream at the linear long wave speed, $Nd/n\pi$, where n is the modal number. The passage of these modes then leads to the flow where the horizontal velocity profile at any vertical section has the same profile as that in the vicinity of the sink. Thus, the selective withdrawal is established. These modes are called columnar disturbance modes, or more briefly, columnar modes or shear fronts whose behavior is one of our main interests in the present study.

To grasp qualitative feature of the linear columnar modes, Pao and Kao [9] applied the hydrostatic approximation to show that these modes travel upstream in the form of horizontal jet-like columns with discontinuous change of their amplitude at the leading regions or fronts. These modes were also studied theoretically and experimentally by McEwan and Baines [21] in connection with an entirely different problem. They found that the fronts of columnar modes are discontinuous initially, but their widths expand as $t^{*1/3}$, where t^* is time after starting the discharge, due to wave dispersion. The effects of $F > 0$ on propagation of columnar modes were also investigated by Pao and Kao [9]. They conducted numerical calculations of the flow when $F > 0$ and concluded that the modes can propagate upstream only if their propagation speed is greater than the average speed of the flow toward the sink. They suggested that the nth mode propagates upstream at the speed

$$\widetilde{C}_n = \frac{Nd}{n\pi} - \frac{Q}{d} = Nd\left(\frac{1}{n\pi} - F\right). \tag{2}$$

Accordingly, the higher modes such that $n > (\pi F)^{-1}$ cannot propagate upstream but are swept out of the sink. This fact was also confirmed by the experiments simultaneously conducted by Kao et al. [10], and supported

for more than twenty years since. In 1995, however, Clarke and Imberger [17] took into account the effect of the modified velocity profile caused by the propagation of the lower columnar modes, and showed that any mode does propagate upstream. They approximated the modified velocity profile by a simple function (the stagnant upper layer and the flowing lower layer with constant shear) and found that the higher modes have the vertical structure different from the trigonometric function so that the character of these modes is totally different from that of the linear modes. According to their study, the higher modes such that $n > (\pi F)^{-1/2}$ also propagate upstream at the speed

$$\widetilde{C}_n = Nd(1-\delta)/n\pi, \tag{3}$$

where $d\delta$ is the withdrawal-layer thickness.

When the length scale and time scale we are concerned with are relatively large, the effect of the earth's rotation must be taken into account (see *figure 1* where $f/2$ is a rotating angular speed of the system). Little attention has previously been paid to the effect of rotation [22–25] that seems to be significant in the oceans or large lakes, etc. [1]. Mcdonald and Imberger [24] studied the line sink flow of a rotating stratified fluid in an unbounded domain. They used the Laplace transform in time to obtain the linear solution and showed that waves generated at the sink destructively interfere due to the low-frequency cutoff f so that the steady-state withdrawal-layer thickness grows with a distance from the sink. They [25] also made use of the solution in an unbounded case to construct the solution in a reservoir of finite depth by applying the method of images to satisfy the boundary conditions of no flow normal to the top and bottom of the reservoir. They, however, resorted to the hydrostatic approximation to simplify the solution in which no waves of short horizontal wavelength are described.

In the present paper, we study the line sink flow of both non-rotating and rotating stratified fluid in a reservoir of finite depth under an assumption that the fluid is incompressible, inviscid, and non-diffusive. We first investigate the behavior of the linear modes ($F \to 0$) theoretically. We use the stationary phase method to obtain an asymptotic solution as $t^* \to \infty$ of these modes which is uniformly valid in space. The solution obtained is subject to no wavelength approximation, unlike previous works, so it describes all wave components that are present. Furthermore, and more importantly, the form of this solution represents the wave nature so convincingly that the propagation phenomena of the individual wave components can be clearly understood. Next, a numerical calculation is conducted to clarify the effect of nonlinearity on the mode propagation. Specifically, the validity of both our linear asymptotic solution and the approximate theory suggested by Clarke and Imberger [17] in describing the mode propagation when $F > 0$ is explored. We also investigate the resultant flow patterns formed by the propagation of these modes. We are especially interested in the withdrawal-layer thickness. The obtained results are compared with those of the previous studies.

In section 2, we shall formulate the equations of motion to show that parameters characterizing the problem are F and f/N. In section 3, we consider the case of $F \to 0$ to study theoretically the behavior of the linear modes. Section 4 gives the numerical method. In section 5, numerical results are presented for flows with $F > 0$, and finally, in section 6, concluding remarks are given.

2. Formulation

Consider a flow inside a horizontally infinite reservoir of finite depth d ($-\infty < x^* < \infty$, $-\infty < y^* < \infty$, $0 < z^* < d$; $x^* - y^* - z^*$ is the Cartesian coordinate system), where a line sink is situated at the bottom along the y^* axis, the gravitational acceleration g acts in the negative z^* direction, and the whole system is rotating at angular speed $f/2$ about the z^* axis (see *figure 1*). The case of a non-rotating system can be treated by putting $f = 0$. Initially, the fluid is quiescent and linearly stratified in the z^* direction so that the initial density

distribution is given by

$$\overline{\rho}(z^*) = \rho_0(1 - \kappa z^*), \tag{4}$$

where ρ_0 is the density at $z^* = 0$ and κ is a positive constant. We are interested here in the flow after starting the discharge $2Q$ per unit length of the line sink at time $t^* = 0$. It is assumed that the fluid is incompressible, inviscid, non-diffusive, and the flow has no y^* dependence. In a rotating system, the Coriolis force induces the flow in the y^* direction so that sidewall, if any, must have some influence on the evolution of the flow. According to Gill [26] and Mcdonald and Imberger [25], however, the effect of the sidewall is confined within a distance of the Rossby radius and further away from the sidewall the flow evolves as if no side boundaries are present. Therefore, in the present study, we consider a simplified problem of the line sink flow with no sidewall. The Boussinesq approximation is also applied assuming that the fluid satisfies $\kappa d \ll 1$, which is often the case of most practical situations. This flow is symmetric with respect to the z^* axis. Therefore we analyze this problem only in the first quadrant of a $x^* - z^*$ plane by imposing the free-slip condition on the z^* axis in the fluid.

We express the time-dependent density distribution $\tilde{\rho}$ as

$$\tilde{\rho}(x^*, z^*, t^*) = \overline{\rho}(z^*) + \rho'(x^*, z^*, t^*), \tag{5}$$

where ρ' is the density fluctuation from its initial value $\overline{\rho}$. We define (u^*, v^*, w^*) as the velocity components in the (x^*, y^*, z^*) directions and introduce the following dimensionless variables

$$\begin{aligned} (u, v, w) &= \left(\frac{u^*}{U_0}, \frac{v^*}{U_0}, \frac{w^*}{U_0}\right), \qquad t = Nt^*, \\ (x, z) &= \left(\frac{x^*}{d}, \frac{z^*}{d}\right), \qquad \rho = \frac{g}{\rho_0 N U_0}\rho', \end{aligned} \tag{6}$$

where $U_0 = Q/d$ and $N = (\kappa g)^{1/2}$ are the average flow speed toward the sink and the constant buoyancy frequency, respectively. From incompressibility of the fluid we can introduce the stream function satisfying $u = \partial\psi/\partial z$ and $w = -\partial\psi/\partial x$ so that the governing dimensionless equations are expressed as

$$\frac{\partial\zeta}{\partial t} + FJ(\zeta, \psi) - \tilde{f}\frac{\partial v}{\partial z} = \frac{\partial\rho}{\partial x}, \tag{7}$$

$$\frac{\partial v}{\partial t} + FJ(v, \psi) + \tilde{f}\frac{\partial\psi}{\partial z} = 0, \tag{8}$$

$$\frac{\partial\rho}{\partial t} + FJ(\rho, \psi) = -\frac{\partial\psi}{\partial x}, \tag{9}$$

$$\zeta = \frac{\partial^2\psi}{\partial x^2} + \frac{\partial^2\psi}{\partial z^2}, \tag{10}$$

where

$$J(a, b) = \frac{\partial a}{\partial x}\frac{\partial b}{\partial z} - \frac{\partial a}{\partial z}\frac{\partial b}{\partial x}.$$

Equation (7) is the vorticity equation derived from cross-differentiating Euler's equations of motion under rotation in the x and z directions. Equation (9) is the condition of incompressibility. These equations (7)–(10) are to be solved under the initial conditions

$$\zeta = 0, \qquad \rho = 0, \qquad v = 0 \quad (x > 0,\ 0 < z < 1) \tag{11}$$

and the boundary conditions

$$\begin{aligned}
&\psi = 0 \qquad (x \geqslant 0,\ z = 0),\\
&\psi = -1 \qquad (x \geqslant 0,\ z = 1),\\
&\psi = -1 \qquad (x = 0,\ 0 < z < 1),\\
&|\psi| < \infty \qquad (x \to \infty,\ 0 < z < 1).
\end{aligned} \tag{12}$$

Now it is clear that the system (7)–(12) is characterized by the two parameters: the Froude number, F, and the dimensionless rotating angular speed, $\tilde{f} = f/N$. In the present study, we assume $\tilde{f} < 1$, as is the case in most practical situations under the earth's rotation.

3. Linear solution

Substituting $F \to 0$ into (7)–(12), we obtain the following linearized equation in terms of ψ governing the small amplitude motion associated with the line sink flow:

$$\frac{\partial^2}{\partial t^2}\nabla^2\psi + \frac{\partial^2\psi}{\partial x^2} + \tilde{f}^2\frac{\partial^2\psi}{\partial z^2} = 0, \tag{13}$$

where $\nabla^2 = \partial^2/\partial x^2 + \partial^2/\partial z^2$. The initial conditions are

$$\nabla^2\psi = 0, \qquad \frac{\partial}{\partial t}\nabla^2\psi = 0 \tag{14}$$

and the boundary conditions are given in (12).

We now apply the technique of separation of variables, and the solution ψ of the system (12)–(14) can be cast into the following form

$$\psi = -z + \sum_{n=1}^{\infty} \psi_n(x,t)\sin n\pi z. \tag{15}$$

Here ψ_n is a function of x and t satisfying the equation

$$\frac{\partial^2}{\partial t^2}\left(\frac{\partial^2\psi_n}{\partial x^2} - n^2\pi^2\psi_n\right) + \frac{\partial^2\psi_n}{\partial x^2} - n^2\pi^2\tilde{f}^2\psi_n = 0 \tag{16}$$

with the initial conditions

$$\psi_n(x,0) = \psi_0\exp(-n\pi x), \qquad \frac{\partial\psi_n}{\partial t}(x,0) = 0 \tag{17}$$

and the boundary conditions

$$\psi_n(0,t) = \psi_0, \qquad \left|\psi_n(\infty,t)\right| < \infty, \tag{18}$$

where

$$\psi_0 = -\frac{2}{n\pi}. \tag{19}$$

The second term on the right-hand side of (15) represents a contribution from the vertical modes $\sin n\pi z$ ($n = 1, 2, \ldots$) where n is the modal number and ψ_n represents an amplitude of the nth mode. The purpose of

the present section is to solve the system (16)–(18), to obtain an asymptotic solution of ψ_n for large t that can exhibit the wave nature clearly.

To obtain such a solution, an integral representation should be constructed, so we introduce the Fourier sine transform in x and the Laplace transform in t, and set

$$\hat{\psi}_n(k,s) = \int_0^\infty \exp(-st)\,\mathrm{d}t \int_0^\infty \psi_n(x,t)\sin kx\,\mathrm{d}x,$$
$$\psi_n(x,t) = \frac{1}{\pi^2 i}\int_0^\infty \sin kx\,\mathrm{d}k \int_{\gamma-i\infty}^{\gamma+i\infty} \hat{\psi}_n(k,s)\exp(st)\,\mathrm{d}s,$$

where γ is a real value that places the path of integration to the right of all singularities of the integrand in the complex s plane. Applying these to (16) and using (17) and (18), we get, after some calculation,

$$\psi_n(x,t) = \psi_0 I(n\pi x, t), \tag{20}$$

where

$$I(n\pi x,t) = \frac{1}{\pi^2 i}\int_0^\infty \frac{k\sin kx}{k^2+n^2\pi^2}\,\mathrm{d}k \int_{\gamma-i\infty}^{\gamma+i\infty} \frac{(s^2+1)\exp(st)}{s\{s-i\omega_0(k)\}\{s+i\omega_0(k)\}}\,\mathrm{d}s \tag{21}$$

and

$$\omega_0(k) = \begin{cases} \dfrac{k}{(k^2+n^2\pi^2)^{1/2}} & (\tilde{f}=0), \\ \left(\dfrac{k^2+n^2\pi^2\tilde{f}^2}{k^2+n^2\pi^2}\right)^{1/2} & (\tilde{f}>0). \end{cases} \tag{22}$$

Carrying out the integration with respect to s, we obtain

$$I(n\pi x,t) = \exp(-n\pi\tilde{f}x) - I_+(n\pi x,t) + I_-(n\pi x,t), \tag{23}$$

where

$$I_\pm(n\pi x,t) = \mathrm{Im}\left[\int_{-\infty}^{\infty} h(k)\exp\{i\chi_\pm(k)t\}\,\mathrm{d}k\right] \tag{24}$$

and

$$h(k) = \frac{n^2\pi(1-\tilde{f}^2)k}{2(k^2+n^2\pi^2)(k^2+n^2\pi^2\tilde{f}^2)}, \tag{25}$$

$$\chi_\pm(k) = \omega_0(k) \pm k\frac{x}{t}. \tag{26}$$

Note that in the case of $\tilde{f}=0$, the paths of integration must be taken to the same side of real axis around a simple pole $k=0$ (see equation (25)) for both I_+ and I_-. Next, we follow Lighthill [27] (see also [28]) to seek an asymptotic solution of I for large t but which is uniformly valid for arbitrary x by the combination of three solutions each of which is valid for $n\pi x < t$, $n\pi x \approx t$, and $n\pi x > t$, respectively. The methods of these analyses are given separately for $\tilde{f}=0$ and $\tilde{f}>0$ in the followings.

3.1. The system under no rigid rotation ($\tilde{f} = 0$)

The stationary points of the integrand of $I_\pm$ are given by solving

$$\chi'_\pm(k) \equiv \frac{\mathrm{d}\chi_\pm}{\mathrm{d}k} = \frac{n^2\pi^2}{(k^2+n^2\pi^2)^{3/2}} \pm \frac{x}{t} = 0, \tag{27}$$

which yields no real stationary points for the phase χ_+. For the phase χ_-, (27) gives

$$k = \pm k_0 \equiv \pm n\pi \left\{ \left(\frac{t}{n\pi x} \right)^{2/3} - 1 \right\}^{1/2} \quad \text{when } n\pi x < t \tag{28}$$

and no real stationary points when $n\pi x > t$.

Here we choose paths of integration passing to the left side of the simple pole $k = 0$. This choice makes I_+ exponentially small as $t \to \infty$ because the path of integration can be raised everywhere so as to give the imaginary part of $\chi_+ t$ a positive value of order t^ε, where ε is a positive small constant. But I_- has a contribution from this pole when $n\pi x > t$ because the path must be lowered everywhere to make the imaginary part of $\chi_- t$ positive. Only in the vicinity of $k = 0$ is the path raised to go round the simple pole $k = 0$ in a clockwise sense, so we find from the residue theorem

$$I_-(n\pi x, t) = -1 \quad \text{for } n\pi x > t. \tag{29}$$

Terms of exponentially small order with respect to t are omitted on the right-hand side of (29) (the same rule will be applied hereafter). Note that there is no contribution from the other poles, $k = \pm n\pi i$, since a path of integration can be taken such that its imaginary part ($\sim t^{\varepsilon-1}/\chi'_\pm(0)$) is smaller than $n\pi$ in order to make the error term [$\sim \exp(-t^\varepsilon)$] exponentially small when t is large.

For $n\pi x < t$, on the other hand, the contribution from the simple pole $k = 0$ vanishes because the path is raised over the range $-k_0 < k < k_0$. Instead, we must estimate the integral in the vicinity of the stationary phase points $k = \pm k_0$. The contribution to I_- from these stationary phase points is obtained by an application of the method shown in [27], sec. 3.7, and it becomes

$$I_-(n\pi x, t) = 2h(k_0) \left(\frac{2\pi}{|\chi''_-(k_0)|t} \right)^{1/2} \sin\left\{ \chi_-(k_0)t - \frac{\pi}{4} \right\} + \mathrm{O}\left(t^{-l/3-7/6}\right) \quad \text{for } n\pi x < t, \tag{30}$$

where

$$\chi''_-(k) = \frac{\mathrm{d}^2\chi_-}{\mathrm{d}k^2} = -\frac{3n^2\pi^2 k}{(k^2+n^2\pi^2)^{5/2}} \tag{31}$$

(see also [28], p. 272 for evaluating the error term in (30)). The constant l appearing in the error term of (30) represents the order of x in terms of t, namely, $x \sim t^l$. For arbitrary values of l ($\leqslant 1$), the first term on the right-hand side of (30) is $\mathrm{O}(t^{l/3-5/6})$, and the solution (30) is valid for $-1/2 < l \leqslant 1$.

When $n\pi x = t$, I_- has only one stationary point $k = 0$ (see (28)), and so we get $\chi''_-(0) = 0$ from (31). Therefore the asymptotic behavior represented by (30) is not valid as $n\pi x \to t$. According to Lighthill [27], sec. 4.11, this point is called a caustic, which is a boundary between a region with a complicated wave pattern, due to interference between two groups of waves and a neighboring region including no waves. In [27], sec. 4.11, the procedure to obtain the asymptotic behavior near the caustic is shown. To avoid singularity at

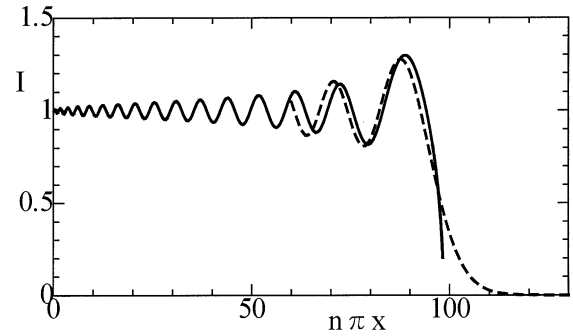

Figure 2. The $n\pi x$ dependence of I at $t = 100$ when $\tilde{f} = 0$. Solid line shows the result by the solution (23) with (30) ($I_+ = 0$). Dashed line shows the result by the solution (23) with (32).

$k = 0$, we first differentiate I_- with respect to $n\pi x$, and then apply his method to $\partial I_-/\partial(n\pi x)$. Thus, we get, after integrating the obtained asymptotic solution of $\partial I_-/\partial(n\pi x)$ with respect to $n\pi x$ under the boundary condition (29) as $n\pi x \to \infty$,

$$I_-(n\pi x, t) = -1 + \int_X^\infty A_i(X')\,\mathrm{d}X'\{1 + \mathrm{O}(t^{-2/3})\} \quad \text{near } n\pi x = t, \tag{32}$$

where

$$X = \left(\frac{2}{3t}\right)^{1/3}(n\pi x - t) \tag{33}$$

and $A_i(X)$ is the Airy integral defined by

$$A_i(X) = \frac{1}{2\pi}\int_{\infty\exp(-(5\pi i/6))}^{\infty\exp(-(\pi i/6))} \exp\left\{-i\left(Xs + \frac{s^3}{3}\right)\right\}\mathrm{d}s. \tag{34}$$

Finally, substituting (29), (30), (32), and $I_+ = 0$ into (23), we get the asymptotic solution of I for large t which is valid for arbitrary x. This profile at $t = 100$ is presented in *figure 2*. From this figure we can see that the modal front propagates horizontally at the dimensionless linear long wave speed, $1/n\pi$. From (32) and (33), the front has its width of $\mathrm{O}(t^{1/3})$ and amplitude of $\mathrm{O}(1)$, which agrees with the results obtained by McEwan and Baines [21]. Behind the front, two types of waves are present. First, the long wave, that is called columnar mode, has its radian frequency $\omega_0 = 0$ and horizontal wavenumber $k = 0$ with its amplitude equal to 1 (see the first term on the right-hand side of (23)). Second, the shorter waves whose ω_0 and k $(= k_0)$ are both larger than zero, have their amplitudes of $\mathrm{O}(x^{1/3}t^{-5/6})$ (see (30) and the statement following (31)).

We now compare our solution of the modal front (32) with that of McEwan and Baines [21]. They used the steepest decent method to obtain the asymptotic behavior of the front as $t \to \infty$. The obtained result is represented by their solution (3.25) and its profile is shown in their *figure 3* (see [21]). However, there exists a discrepancy between their result and ours. For instance, no oscillatory profile can be seen in their result (see their *figure 3*). The reason for the discrepancy is caused by a problem in their analytical process: the saddle point $s = s_1$ on which an integral is evaluated is too close to a singularity point $s = 0$. It will be shown later that our result agrees well with the numerical results in the limit $F \to 0$ (see section 5.1 below).

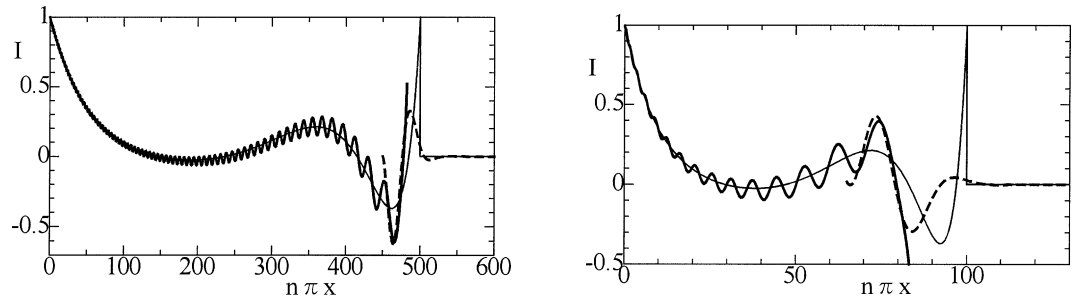

Figure 3. The $n\pi x$ dependence of I at $\tilde{f}t = 10$: (a) $\tilde{f} = 0.02$; (b) $\tilde{f} = 0.1$. Broad solid lines show the results by the solution (35) with (40) and broad dashed lines show the results by the solution (35) with (45). Thin solid lines show the results by the solution under the hydrostatic approximation obtained by Mcdonald and Imberger [22].

3.2. The system under rigid rotation ($\tilde{f} > 0$)

When $\tilde{f} > 0$, (23) becomes a simplified form:

$$I(n\pi x, t) = \exp(-n\pi \tilde{f} x) + 2I_-(n\pi x, t). \tag{35}$$

The stationary points of the integrand of I_- are given by $\chi'_-(k) = 0$, which yields the following equation

$$K^4 + (3 + \tilde{f}^2)K^3 + 3(1 + \tilde{f}^2)K^2 + \left\{1 + 3\tilde{f}^2 - (1 - \tilde{f}^2)^2\left(\frac{t}{n\pi x}\right)^2\right\}K + \tilde{f}^2 = 0, \tag{36}$$

where

$$K = \frac{k^2}{n^2\pi^2}. \tag{37}$$

Solving (36), we obtain two positive real stationary points $k = k_1,\ k_2\ (0 < k_1 < k_2)$ for $n\pi x < t_f$ and no real stationary points for $n\pi x > t_f$ where

$$t_f = \frac{n^3\pi^3 k_3(1 - \tilde{f}^2)t}{(k_3^2 + n^2\pi^2)^{3/2}(k_3^2 + n^2\pi^2\tilde{f}^2)^{1/2}} \tag{38}$$

and

$$k_3 = n\pi\left[\frac{\tilde{f}}{3}\{(3 + \tilde{f}^2)^{1/2} - \tilde{f}\}\right]^{1/2}. \tag{39}$$

The contribution to I_- from these stationary points is again obtained by an application of the method in [27], sec. 3.7, and it becomes

$$I_-(n\pi x, t) = I_1(n\pi x, t) + I_2(n\pi x, t) \quad \text{for } n\pi x < t_f, \tag{40}$$

where

$$I_1(n\pi x, t) = A(k_1)\sin\left\{\chi_-(k_1)t + \frac{\pi}{4}\right\} + \mathrm{O}\left(t^{l-5/2}\right), \tag{41}$$

$$I_2(n\pi x,t) = A(k_2)\sin\left\{\chi_-(k_2)t - \frac{\pi}{4}\right\} + \mathrm{O}\left(t^{-l/3-7/6}\right) \tag{42}$$

and

$$A(k) = h(k)\left(\frac{2\pi}{|\chi_-''(k)|t}\right)^{1/2}, \tag{43}$$

$$\chi_-''(k) = -\frac{n^2\pi^2(1-\tilde{f}^2)(k^2-k_3^2)[3k^2+n^2\pi^2\tilde{f}\{(3+\tilde{f}^2)^{1/2}+\tilde{f}\}]}{(k^2+n^2\pi^2)^{5/2}(k^2+n^2\pi^2\tilde{f}^2)^{3/2}} \tag{44}$$

(see also [28], p. 272, for evaluating the error terms in (41) and (42)). (41) and (42) represent the motions of the longer and the shorter wave components, respectively. The longer waves have their amplitude of $\mathrm{O}(t^{l-3/2})$ while the shorter ones have that of $\mathrm{O}(t^{l/3-5/6})$. The solution (40) is valid for $-1/2 < l \leqslant 1$.

When $n\pi x = t_f$, I_- has only one real stationary point, $k = k_3$ (from (36)). We then obtain $\chi_-''(k_3) = 0$ from (44) so that the solution (40) is not valid as $n\pi x \to t_f$ (see (43)). In this region, which is near a caustic, the asymptotic solution of I_- is obtained by a straightforward application of the method introduced in [27], sec. 4.11, as in the case of $\tilde{f} = 0$, which gives

$$I_-(n\pi x,t) = 2\pi h(k_3)\left(\frac{-2}{\chi_-^{(3)}(k_3)t}\right)^{1/3} A_i(X)\sin\{\chi_-(k_3)t\} \times \{1+\mathrm{O}(t^{-1/3})\} \quad \text{near } n\pi x = t_f, \tag{45}$$

where

$$X = \left(\frac{-2}{n^3\pi^3\chi_-^{(3)}(k_3)t}\right)^{1/3}(n\pi x - t_f), \tag{46}$$

$$\chi_-^{(3)}(k) = \frac{\mathrm{d}^3\chi_-}{\mathrm{d}k^3}.$$

Substituting $I_- = 0$ (for $n\pi x > t_f$), (40), and (45) into (35), we obtain the asymptotic solution of I for large t which is valid for arbitrary x. The profiles of I at $\tilde{f}t = 10$ for $\tilde{f} = 0.02$ and 0.1 are presented in *figure 3*. From these figures (especially from *figure 3(b)*) we can find that the nth modal front propagates horizontally at the speed smaller than $1/n\pi$, or the long wave speed of the nth internal wave mode. This is in accordance with the linear dispersion relationship (22) which gives the horizontal group velocity of the nth inertial gravity wave mode as

$$\frac{\mathrm{d}\omega_0}{\mathrm{d}k} = \frac{n^2\pi^2k(1-\tilde{f}^2)}{(k^2+n^2\pi^2)^{3/2}(k^2+n^2\pi^2\tilde{f}^2)^{1/2}} \tag{47}$$

whose maximum value with respect to k is a decreasing function of $\tilde{f}$. Now waves of the maximum group velocity satisfy $\mathrm{d}^2\omega_0/\mathrm{d}k^2 = \chi_-''(k) = 0$, which gives $k = k_3$ (> 0) from (44). Therefore, in the system under rigid rotation, the modal front is constructed by waves whose ω_0 and k ($= k_3$) are both larger than zero. The amplitude of this modal front decreases as $t^{-1/3}$ (see (45)), unlike the case of $\tilde{f} = 0$ where it is O(1). However, its width expands as $t^{1/3}$ (see (46)), which is the same order as in the case of $\tilde{f} = 0$.

Behind the front, two types of waves are present. First, the longer waves, that resemble inertial waves, have horizontal wavenumber k_1, which is smaller than that of the front, k_3. Second, the shorter waves, that resemble internal waves, have horizontal wavenumber k_2, which is larger than k_3. Both k_1 and k_2 are dependent on $n\pi x/t$ (see (36)). k_1 and k_2 change their values from k_3 to zero and infinity, respectively as $n\pi x/t$ decreases. So the

difference in value between these two wavenumbers increases as $n\pi x/t$ decreases. The amplitudes of these waves are $O(xt^{-3/2})$ and $O(x^{1/3}t^{-5/6})$ for the longer and the shorter waves, respectively (see the statement following (44)).

Figure 3 shows that I approaches the fixed boundary value 1 as $x \to 0$. This indicates that some disturbances of frequency zero must be present in the vicinity of the sink. Under rigid rotation of the whole system, the linear dispersion relationship (22) requires that inertial gravity waves must have their dimensionless radian frequency larger than $\tilde{f}$. Therefore not waves but evanescent disturbances are generated in response to the force of frequency zero, or, in the present problem, the constant withdrawal. The amplitude of these evanescent disturbances decreases exponentially with x and they cannot reach far upstream (see the first term on the right-hand side of (35)).

Profiles of the solution under the hydrostatic approximation obtained by Mcdonald and Imberger [25] are also presented in *figure 3*. This approximation is equivalent to ignoring vertical acceleration of fluids, or neglecting the first term on the left-hand side of (16), which corresponds to the long wave approximation. *Figure 3* shows that their results agree well with our asymptotic solutions except for the following three points: (i) there exist no shorter wave components; (ii) the amplitude is discontinuous at the front; (iii) the maximum propagation speed is $1/n\pi$ independent of $\tilde{f}$.

4. Numerical method

The numerical method used to solve the system of basic equations (7)–(12) is a spectral collocation method [29]. Since $\psi + z$, ρ, and ζ become zero at the top and bottom boundaries $z = 0, 1$, these variables are expanded in a Fourier sine series in the z direction. In contrast, v is expanded in a Fourier cosine series, since its z derivative is zero at $z = 0, 1$ under the Boussinesq approximation. In the x direction, a Chebyshev series is used for all variables. The computational domain is $0 < x < \infty,\ 0 < z < 1$ so that the exponential mapping [29] is used in the x direction expressed by

$$\begin{aligned} x_j &= -L \ln\left(\frac{1-\xi_j}{2}\right), \\ \xi_j &= \cos\frac{\pi j}{J} \quad (j = 0, 1, \ldots, J), \end{aligned} \tag{48}$$

where J is the number of total collocation points in the x direction and L sets the length scale of the mapping. Thus, the collocation points are concentrated toward the sink and the higher modes near the sink are calculated with higher accuracy. It should be noted, however, that these collocation points are coarse far upstream because of the stretching of the x coordinate. Therefore the possible calculation time is limited by the time before the first mode arrives at the location, where the collocation points are not distributed enough to capture its motion. In this study, two kinds of collocation points are used depending on the value of $\tilde{f}$: $(J, M, L) = (256, 128, 8)$ for $\tilde{f} = 0$ and $(J, M, L) = (512, 64, 32)$ for $\tilde{f} > 0$ where M is the number of total points in the z direction. When $\tilde{f} = 0$, large M is employed, since one of our interests lies in the motion of the higher modes. When $\tilde{f} > 0$, large J and L are employed, since long times are required to study the effects of the slow rigid rotation ($0 < \tilde{f} \leqslant 0.1$). Calculations are conducted until the first mode arrives at $x = 45$ where $\Delta x_j \equiv x_j - x_{j-1} = 1.5$ for the former case, and at $x = 160$ where $\Delta x_j = 2.4$ for the latter case. It may appear that Δx_j is too large to capture the motion of the first mode. However, this modal front has slow variation with respect to x and as time increases its width expands as $t^{1/3}$ according to McEwan and Baines [21] and the linear solution obtained in section 3 of the present study. In fact, the authors have tested finer grids and no quantitative differences were found in the computational results.

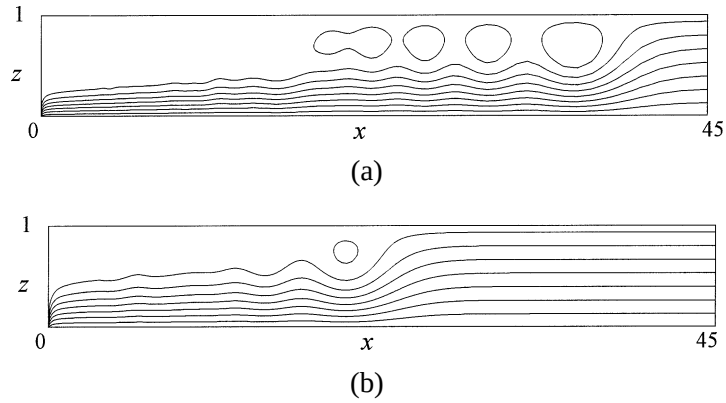

Figure 4. Streamlines at $t = 150$ ($\tilde{f} = 0$): (a) $F = 0.05$; (b) $F = 0.16$.

A fourth-order Runge–Kutta method is used to timestep the equations. The elliptic equation (10) is solved using a direct solution technique [29]. To avoid singularity at the sink, we use the following continuous function for the boundary condition of ψ at $x = 0$ [11]:

$$\psi = -\frac{\mathrm{erf}(az)}{\mathrm{erf}(a)} \tag{49}$$

instead of the third condition of (12). Here erf is the error function. The condition (49) approaches that of the sink flow as a increases. Such a distributed sink is valid when $F > 0$, since the withdrawal-layer thickness increases abruptly in the close vicinity of the sink where the nonlinear advective effect overcomes the buoyancy effect (see also section 5). As F increases, this nonlinear effect becomes larger and the withdrawal-layer thickness can increase more in response to that. Thus, the smaller a can be used for calculating the flow of larger F. In the present study, we put $a = 15$ for $0.02 \leqslant F \leqslant 0.1$ and $a = 10$ for $F > 0.1$. We have tested several cases with the larger values of a and found no quantitative differences in the computational results over the region $x > 3$.

5. Numerical results

5.1. *The system under no rigid rotation* ($\tilde{f} = 0$)

In *figure 4*, streamlines at $t = 150$ for $F = 0.05$ and 0.16 are presented. From these figures we can see that the stagnant region spreads upstream at the linear long wave speed of the first mode, $1/\pi - F$ (note that $(1/\pi - F) \times 150 = 40$ and 24 for $F = 0.05$ and 0.16, respectively), as predicted by Pao and Kao [9] (hereafter referred as PK) (see (2)). To see more clearly the behavior of the individual modes, we define the strength of each mode by

$$u_n(x, t) = 2 \int_0^1 u \cos n\pi z \, \mathrm{d}z. \tag{50}$$

The obtained value of u_1 at $t = 150$ is presented in *figure 5*. Also shown is the value of u_1 calculated from the linear asymptotic solution (23) with (30) and (32) (note that $u_n = -2I$). From this figure we see that u_1 for arbitrary F shows similar profile to that for $F \to 0$. As F increases, however, the phase is located downstream side, which is simply due to the effect of the average flow velocity ($= -F$) toward the sink. It is also seen that

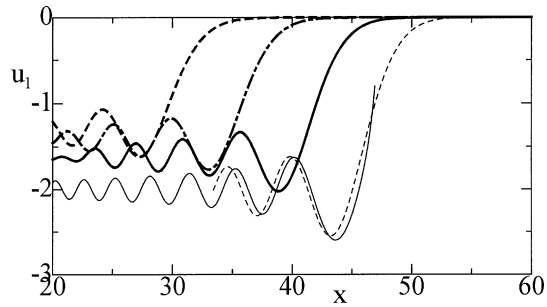

Figure 5. The x dependence of u_1 at $t = 150$ ($\tilde{f} = 0$). Broad lines show the numerical results for $F = 0.03$ (solid line), 0.07 (chain line), and 0.11 (dashed line). Thin lines show the result by the linear solution (23) with (30) (solid line) and (32) (dashed line). (Note that $u_1 = -2I$.)

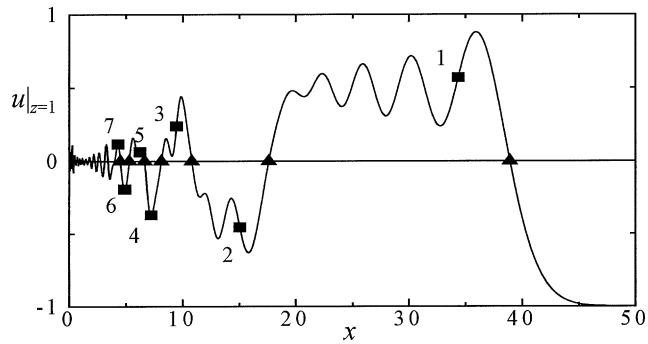

Figure 6. The x dependence of $u|_{z=1}$ at time $t = 150$ when $F = 0.05$ ($\tilde{f} = 0$). The solid square marked n indicates the position of the middle point between the first peak and trough [at the peak (trough) when no trough (peak) is present] of the nth modal strength behind its front. The solid triangles indicate the positions of the individual modal fronts.

the absolute value of the modal strength uniformly decreases as F increases. In fact, this trend, which could be seen even for the higher modes, was also observed in experiments conducted by Monismith and Imberger [16]. We give the physical interpretation of this phenomenon as follows.

In close vicinity of the sink, the flow speed is so large that the nonlinear advective effect overcomes the buoyancy effect. Therefore the withdrawal-layer thickness grows with x until the buoyancy effect becomes predominant. Once the buoyancy effect becomes predominant, say at $x = x_b$, the flow for $x > x_b$ changes by the propagation of the internal wave modes, and the motion of these modes is influenced by the velocity distribution (here defined as $u_b(z)$) at $x = x_b$. That is, the horizontal velocity distribution at $x = x_b$ serves as the boundary condition on u for $x > x_b$, and $u_b(z)$ can be decomposed into its modal components, each of which serves as a boundary condition for one mode of motion. The profile of $u_b(z)$ approaches that of uniform flow as F increases because the withdrawal-layer thickness must increase more in response to the larger advective effect relative to the buoyancy effect. Consequently, as F increases, the amplitude of each modal component of $u_b(z)$ decreases, and in effect, the strength of the individual modes for $x > x_b$ also decreases.

The modal strength defined by (50) is not valid to see the behavior of columnar modes $n \geqslant 2$ because their modal functions are not necessarily trigonometric, as suggested by Clarke and Imberger [17] (hereafter referred as CI). Here we try to determine the frontal positions of these modes from the profile of u on the upper boundary $z = 1$ ($\equiv u|_{z=1}$). The x dependence of $u|_{z=1}$ for $F = 0.05$ at $t = 150$ is presented in *figure 6*. From this figure we see that $u|_{z=1}$ oscillates around zero. Our supposition is that the change in sign of $u|_{z=1}$ indicates an arrival of the next higher mode. To verify this idea, we mark the solid squares at the middle point between the first peak and trough (at the peak (trough) when no trough (peak) is present) after $u|_{z=1}$ changes its sign when tracing

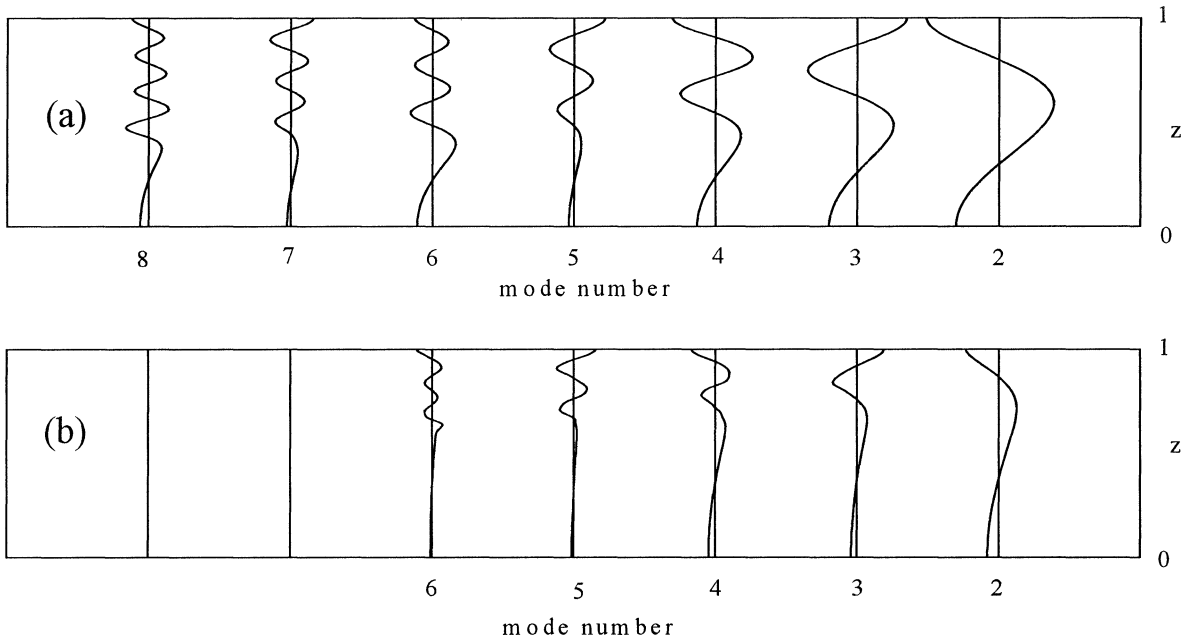

Figure 7. Horizontal velocity profiles of the individual modes versus z: (a) $F = 0.05$; (b) $F = 0.16$. The numbers presented just below each profile indicate the corresponding modal numbers.

downstream along the curve of $u|_{z=1}$. These marks are numbered consecutively as shown in *figure 6*, and then we subtract the velocity profile $u(z)$ marked $n-1$ from that marked n to obtain the velocity profile of the nth columnar mode, which is shown in *figure 7*(*a*) (note that a similar method was used by Silvester [13] to obtain the vertical structure of the individual modes in his experiments). According to this figure, the number of nodal points of the obtained velocity profile agrees with the corresponding modal number of our supposition presented just below the individual profiles. Therefore we can say that the change in sign of $u|_{z=1}$ indicates an arrival of the next higher modes and *figure 7*(*a*) describes the velocity profile of each columnar mode correctly.

Also shown in *figure 7* are the corresponding profiles for $F = 0.16$ (*figure 7*(*b*)). From these profiles we can see that the strength of each columnar mode decreases as F increases for a given modal number. It is also seen that the horizontal velocity of any mode is always directed toward the sink at the intake level ($z = 0$), unlike the case of point sink flow [20]. As for the modal structure, it is not trigonometric and agrees well with the suggestion by Clarke and Imberger [17] in the following three points. First, the vertical length scale of the flowing lower layer increases as F increases. Second, this length scale is almost independent of the modal number for the higher modes. Third, the velocity profile is simply trigonometric in the upper layer.

To examine the propagation speed of the individual modal fronts, we need to know the time dependent positions of each front. We defined these positions as the x coordinate where $u|_{z=1}$ becomes zero (for reference, these positions for $F = 0.05$ at $t = 150$ are marked by the solid triangles in *figure 6*) and plotted these positions for a given n as a function of t every $t = 10$ over $30 \leqslant t \leqslant 150$. Then we drew a line fitting these data using the method of least squares and the gradient of this line was defined as the dimensionless propagation speed of the nth modal front ($\equiv C_n$). The obtained values of C_n are plotted as a function of the reciprocal of the modal number $1/n$ in *figure 8*. From this figure we see that C_n is proportional to $1/n$ if n is large. The solid line shows the prediction by Clarke and Imberger [17], or the result given by (3) with $\delta = 1.5F^{1/2}$ (see (51) below). The dashed line shows the prediction by Pao and Kao [9], or the result given by (2). Both are for $F = 0.05$. For the higher

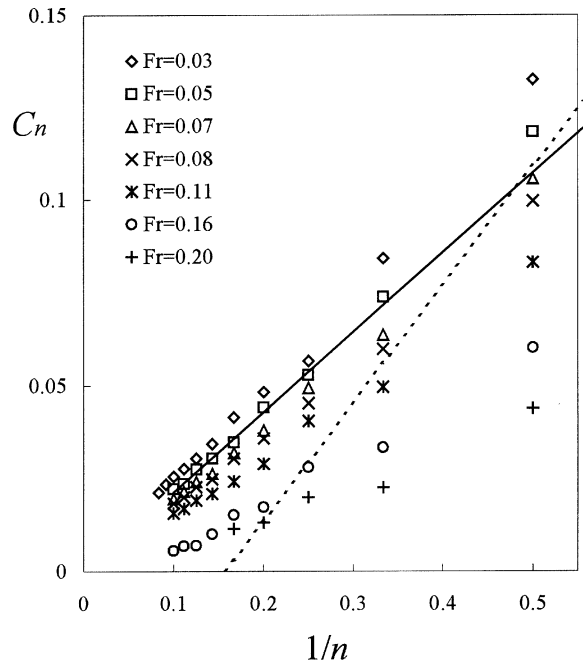

Figure 8. The dimensionless propagation speed of the nth modal front, C_n, as a function of $1/n$. Solid line shows the prediction by Clarke and Imberger, or the result given by (3) with $\delta = 1.5F^{1/2}$ ($F = 0.05$). The dashed line shows the prediction by Pao and Kao, or the result given by (2) ($F = 0.05$).

modes $n \geqslant 3$, we can see a good agreement between our numerical results and the prediction by Clarke and Imberger [17], while an agreement between the numerical results and the prediction by Pao and Kao [9] is poor.

Next, we investigate the effect of the individual modes on the withdrawal-layer thickness. Defining δ as the vertical coordinate z at which the horizontal velocity has dropped to zero, we have plotted in *figure 9* the values of $\delta F^{-1/2}$ at the x coordinate between the first peak and trough of the individual modal strengths behind their front (examples of these positions are shown by solid squares in *figure 6*). In *figure 9*, the abscissa is n and the data used are those at $t = 150$. Only the data in the region $x > 3$ were used to avoid the near-sink effect. From this figure it is found that $\delta F^{-1/2}$ asymptotes to some constant value as n increases. This figure suggests that

$$\delta = bF^{1/2} \quad (b = 1.5 \sim 1.6) \tag{51}$$

is a good description of the steady-state dimensionless withdrawal-layer thickness.

According to the prior works, Kao [7] obtained $\delta = 1.74F^{1/2}$ from his theoretical solution assuming that a dividing streamline separates the stagnant upper layer and the flowing lower layer at the steady state. Debler [3] suggested $\delta = 1.89F^{1/2}$ from his experiments. Pao and Kao [9] and Kao et al. [10] both found $\delta_{1/12} = 1.83F^{1/2}$ from their numerical calculations and experiments (note that they defined the withdrawal-layer thickness as the z coordinate at which u has dropped to $1/12$ the value at $z = 0$ so that their value of δ becomes larger when our definition is applied). If we quantitatively compare these results with our numerical result (51), it is found that the results of all previous studies overestimate the withdrawal-layer thickness. The reasons are considered to be the followings. Kao's steady-state solutions, indeed, permit other solutions with the thinner flowing lower layer [7]. Therefore the withdrawal-layer thickness may take the smaller value than suggested by him. The numerical calculations by Pao and Kao [9] were conducted using the first-order upwind finite difference scheme with only 20 grids in the z direction so that the effect of artificial viscosity is not negligible. Debler [3] and Kao et al. [10] conducted their experiments setting parameters such that the flow is subject to

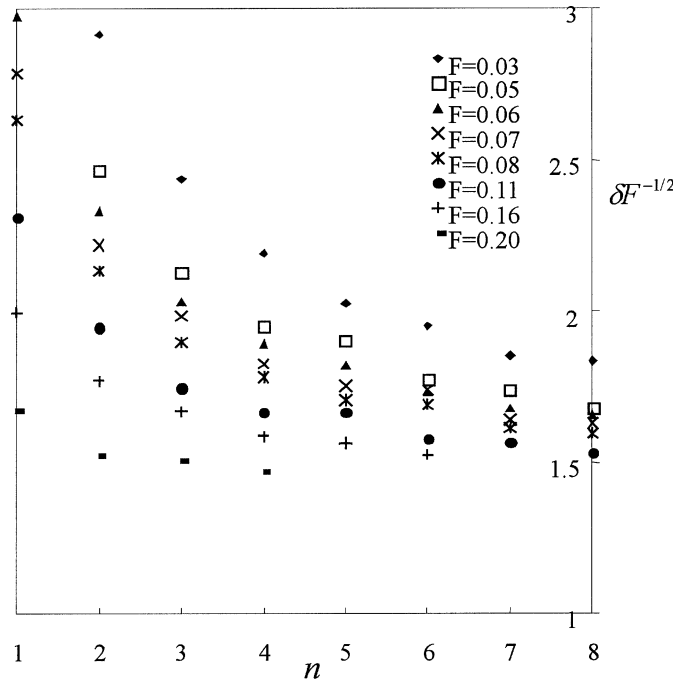

Figure 9. The dimensionless withdrawal-layer thickness $\delta F^{-1/2}$ at the position x between the first peak and trough [at the peak (trough) when no trough (peak) is present] of the nth modal strength behind its front ($1 \leqslant n \leqslant 8$).

little viscous effect. But real fluid possesses some viscosity and we shall see that such a viscosity, however small, has considerable effect on the propagation of the higher modes.

According to Clarke and Imberger [17] and Monismith and Imberger [16], a columnar mode of dimensionless vertical wavelength λ will be damped by viscosity in a distance $x_d = \sqrt{Gr}C_n\lambda^2/4\pi^2$ where $Gr = N^2d^4/\nu^2$ is the Grashof number and ν is the dynamic viscosity. When the mode possesses its vertical structure as shown in *figure 7*, Clarke and Imberger [17] argued that λ is given by the vertical wavelength of the mode in the upper layer. If, as an example, we calculate the value of x_d for mode $n = 4$ in the case of large Grashof number 10^9 (which corresponds to the maximum Grashof number conducted in the experiments by Kao et al. [10]), we obtain $x_d = 6.8$, 2.7, and 1.5 for $F = 0.05,\ 0.11$, and 0.16, respectively. These results indicate that the higher modes are significantly damped even by small viscosity, which is the reason why the withdrawal-layer thickness became larger in their experiments.

Consideration of such a viscous effect also leads us to get the possible reason why Pao and Kao [9], in their numerical studies, wrongly concluded that the number of modes which propagate upstream in an inviscid fluid, decreases as F increases simply by the advective effect. As noted above, the numerical calculations by Pao and Kao cannot ignore the effect of artificial viscosity, and so x_d becomes smaller as F increases, since the vertical structure of the higher modes is modified such that λ and C_n become smaller as F increases for a given n. Thus, in their numerical results, the number of modes arriving at any given location decreases as F increases, which they have misunderstood as caused by the advective effect.

5.2. The system under rigid rotation ($\tilde{f} > 0$)

In *figure 10*, streamlines over the region $0 < x < 7$ at $\tilde{f}t = 10$ are presented for various sets of parameters $(\tilde{f}, F)$. It is found that the withdrawal layer grows in thickness and the flow asymptotes to a uniform flow

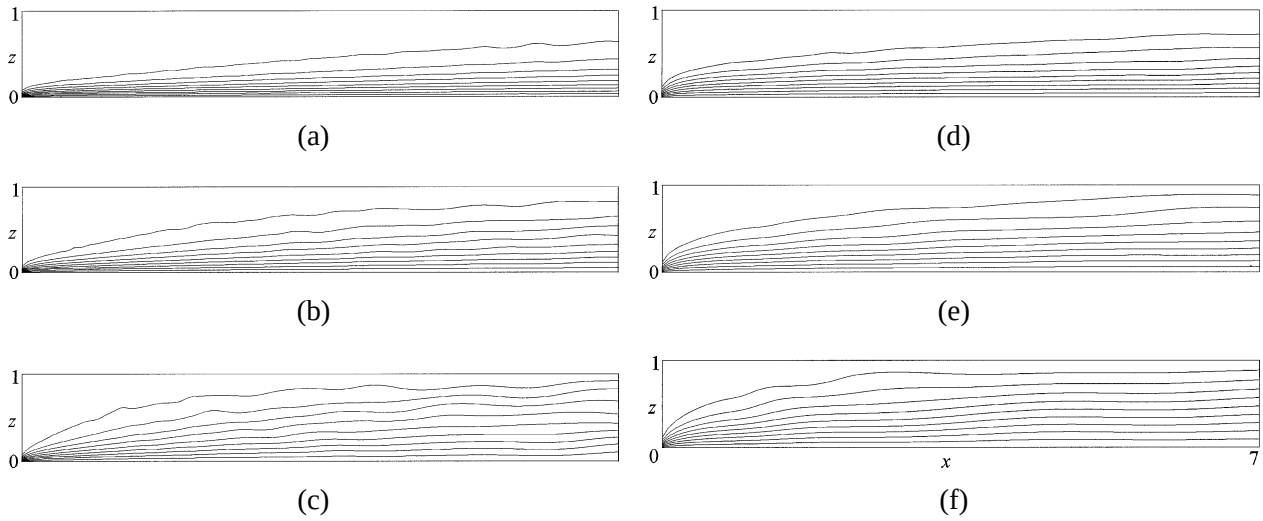

Figure 10. Streamlines at $\tilde{f}t = 10$ near the sink ($0 < x < 7$). The parameters $(\tilde{f}, F)$ are: (a) $(0.02, 0.02)$; (b) $(0.05, 0.02)$; (c) $(0.1, 0.02)$; (d) $(0.02, 0.11)$; (e) $(0.05, 0.11)$; (f) $(0.1, 0.11)$.

as x increases, unlike the case of $\tilde{f} = 0$. This fact is attributed to the requirement by the linear dispersion relationship that modes of frequency zero are not waves but evanescent disturbances so that their amplitude decreases exponentially with x and they cannot reach far upstream (see the first term on the right-hand side of (35)). Thus, the permanent change to the velocity profile virtually disappears by $x = (\pi \tilde{f})^{-1}$, i.e. a distance from the sink of the Rossby radius of the first mode, and so the vertical structure of modes must be trigonometric at $x \gg (\pi \tilde{f})^{-1}$. Therefore the strength of each mode defined by (50) is expected to be valid to see the behavior of the individual modes at $x \gg (\pi \tilde{f})^{-1}$.

The obtained values of u_1 and u_2 at $\tilde{f}t = 10$ are presented in *figure 11*. Also shown are the corresponding plots of u_1 and u_2 calculated from the linear solution (35) with (40) and (45) (note that $u_n = -2I$). From this figure we see that both u_1 and u_2 for arbitrary F show similar profiles to those of the linear theory ($F = 0$) in the region $x \gg (\pi \tilde{f})^{-1}$. According to the linear theory, the front of the nth mode propagates upstream at the speed

$$C_n = \frac{C(\tilde{f})}{n\pi} - F, \tag{52}$$

where $C(\tilde{f})/n\pi$ is the maximum horizontal group velocity of the nth mode obtained by substituting $k = k_3$ (see (39) for the specific form of k_3) into (47). For example, we obtain $C(0.02) = 0.97$ and $C(0.1) = 0.84$. In *figure 11*, the positions of each modal front predicted by (52) are marked by the arrows and we can see a good agreement with the frontal positions of the corresponding numerical results. In fact, the authors have checked the other modes and found that this agreement is also realized for any mode whose front is located at $x \gg (\pi \tilde{f})^{-1}$. Consequently we can say that any mode in the region $x \gg (\pi \tilde{f})^{-1}$ can be well described by the linear theory if we incorporate the following two effects of $F > 0$: the slower propagation speed due to the average flow velocity ($= -F$) and the decrease of the modal strength.

To investigate the withdrawal-layer thickness, we here introduce a new definition because, as seen from *figure 10*, the upper stagnant region shrinks significantly due to rigid rotation of the system, and thus, δ of the previous definition takes a constant value 1 for most part of the region. Therefore it is defined as the vertical coordinate z at which the horizontal velocity has dropped to half the value at $z = 0$ ($\equiv \delta_{1/2}$). This definition was

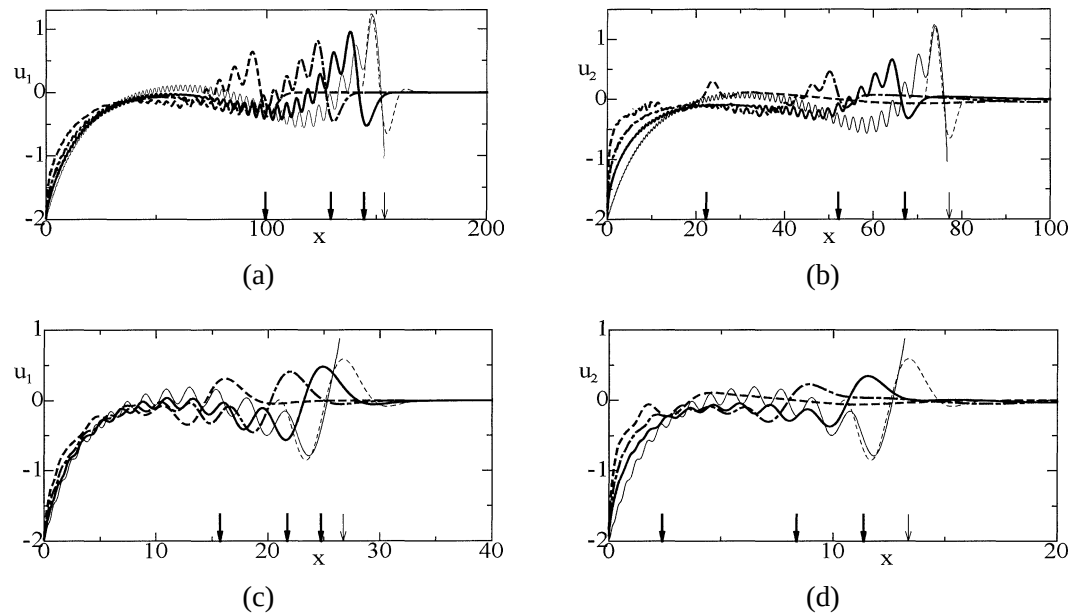

Figure 11. The x dependence of u_n at time $\tilde{f}t = 10$: (a) $(\tilde{f}, n) = (0.02,\ 1)$; (b) (0.02, 2); (c) (0.1, 1); (d) (0.1, 2). Broad lines show the numerical results for $F = 0.02$ (solid line), 0.05 (chain line), and 0.11 (dashed line). Thin lines show the result by the linear solution (35) with (40) (solid line) and (45) (dashed line) (note that $u_n = -2I$). The arrows show the positions of each modal front predicted by (52).

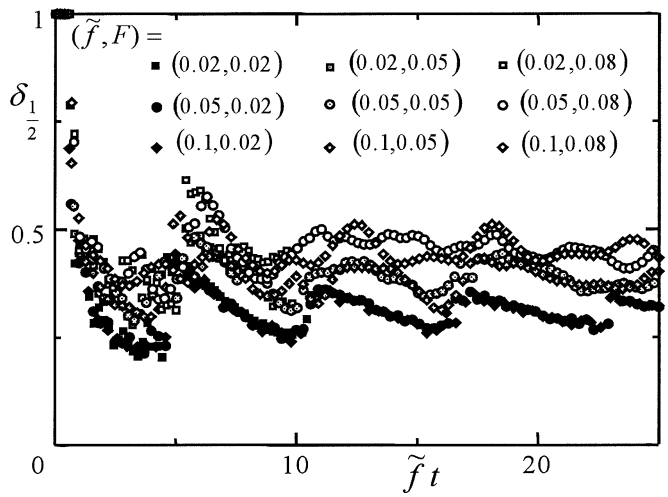

Figure 12. The time $(\tilde{f}t)$ dependence of $\delta_{1/2}$ at $\tilde{f}x = 0.2$.

also used by Imberger et al. [8]. In *figure 12*, the time dependence of $\delta_{1/2}$ at $\tilde{f}x = 0.2$ is presented as a function of $\tilde{f}t$. From this figure we see that $\delta_{1/2}$ oscillates with an approximate period of $\tilde{f}t = 6$, although profiles show some scatter for large F. This oscillation is due to the propagation of the inertial gravity waves. These waves have the low dimensionless frequency cutoff $\tilde{f}$ (see (22)). We can find a good agreement between their period $\tilde{f}t = 2\pi$ and the oscillation period of $\delta_{1/2}$, $\tilde{f}t = 6$. When the system is not rotating, such an oscillation is not detected and $\delta_{1/2}$ monotonically asymptotes to a constant value $0.9F^{1/2}$, which is obtained from the numerical results for $\tilde{f} = 0$.

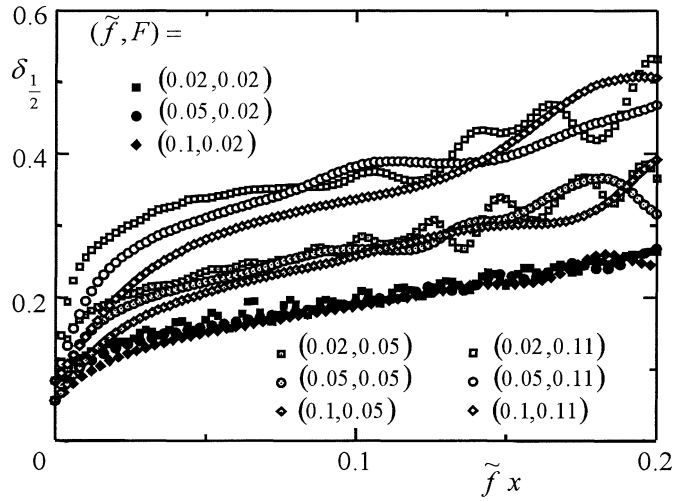

Figure 13. The $\tilde{f}x$ dependence of $\delta_{1/2}$ at time $\tilde{f}t = 10$.

Figure 13 shows the $\tilde{f}x$ dependence of $\delta_{1/2}$ at $\tilde{f}t = 10$. According to this figure, $\delta_{1/2}$ increases with $\tilde{f}x$ due to the effect of rotation. We also see that the gradient of every profile is independent of F except in the close vicinity of the sink where the nonlinear advective effect is predominant. This indicates that the nonlinear effect is confined to the close vicinity of the sink, say $x < x_b$, and the flow for $x > x_b$ changes by spreading upstream of the evanescent disturbances and the inertial gravity waves. Therefore it is expected that the combined effects of nonlinearity and rotation is represented by summation of these two effects. Thus, we obtain

$$\delta_{1/2} = 0.9F^{1/2} + A(\tilde{f}t) \times \tilde{f}x, \tag{53}$$

where $A(\tilde{f}t)$ is a function of $\tilde{f}t$ which represents the variation of $\delta_{1/2}$ with respect to time caused by the propagation of the inertial gravity waves. As time increases, this function is expected to asymptote to a final constant value 1 whose contribution comes from the evanescent disturbances represented by the first term on the right-hand side of (35). When $\tilde{f}x \ll F^{1/2}$ or $\tilde{f}x \gg F^{1/2}$, $\delta_{1/2}$ in (53) agrees with the steady-state thickness of the corresponding regime, obtained by scaling analysis [24]. However, an important point that should be noted here is that the transient behavior represented by $A(\tilde{f}t)$ can have substantial effects on estimating the withdrawal-layer thickness. For instance, $\tilde{f}t = 6$ corresponds to approximately 16 hours under the earth's rotation at middle latitude and $\delta_{1/2}$ substantially changes its value within that period according to *figure 12*. Therefore when the withdrawal is continued for a period as the order of several hours, it is essential to consider the unsteady aspect of the flow caused by the propagation of the inertial gravity waves.

6. Concluding remarks

We have studied the line sink flow of both non-rotating and rotating stratified fluid in a reservoir of finite depth. The main results of the present study are summarized as follows.

We first considered the case of $F \to 0$ to obtain the linear asymptotic solution for large t. The obtained solution is valid for arbitrary x and represents the wave nature clearly. When $\tilde{f} = 0$, the nth modal front, whose amplitude is O(1), propagates upstream at the linear long wave speed $1/n\pi$. Behind the front, the long wave and the shorter waves are present. The long wave has its amplitude equal to the boundary value and the shorter

waves have their amplitude of $O(x^{1/3}t^{-5/6})$. When $\tilde{f} > 0$, the nth modal front, whose amplitude decreases as $t^{-1/3}$, propagates upstream at the speed smaller than $1/n\pi$. Behind the front, the longer and the shorter waves are present and their amplitudes are $O(xt^{-3/2})$ and $O(x^{1/3}t^{-5/6})$, respectively. In the vicinity of the sink, the evanescent disturbances are present with its amplitude decreasing exponentially with a distance from the sink.

Next, numerical calculations were made to clarify the effect of nonlinearity on the mode propagation. The modal strength decreases as F increases for a given modal number. All the first modes and any mode in the region $x \gg (\pi \tilde{f})^{-1}$ can be well described by the linear solution if we incorporate the following two effects of $F > 0$, that is, the slower propagation speed due to the average flow velocity ($= -F$) and decrease of the modal strength. When $\tilde{f} = 0$, the higher modes were found to be well described by the approximate theory of Clarke and Imberger [17].

Finally, we have examined the withdrawal-layer thickness. Every time the higher columnar modes arrive, in the case of $\tilde{f} = 0$, the thickness asymptotes to some constant value which is smaller than the result of the previous studies. The difference is attributed to small viscosity that prevents the higher modes from propagating upstream. When $\tilde{f} > 0$, the withdrawal-layer thickness oscillates with an approximate period of $\tilde{f}t = 6$ due to propagation of the inertial gravity waves. It was suggested that this unsteadiness can be important factor in estimating the withdrawal-layer thickness.

References

[1] Imberger J., Patterson J.C., Physical limnology, Adv. Appl. Mech. 27 (1990) 303–475.
[2] Yih C.-S., On the flow of a stratified fluid, in: Proc. 3rd U.S. Nat. Congr. Appl. Mech., New York, 1958, pp. 857–861.
[3] Debler W.R., Stratified flow into a line sink, J. Eng. Mech.-ASCE 85 (1959) 51–65.
[4] Trustrum K., Rotating and stratified fluid flow, J. Fluid Mech. 19 (1964) 415–432.
[5] Kao T.W., A free-streamline solution for stratified flow into a line sink, J. Fluid Mech. 21 (1965) 535–543.
[6] Koh R.C.Y., Viscous stratified flow toward a sink, J. Fluid Mech. 24 (1966) 555–575.
[7] Kao T.W., Free stream line theory for inviscid stratified flow into a line sink, Phys. Fluids 13 (1970) 558–564.
[8] Imberger J., Two-dimensional sink flow of a stratified fluid contained in a duct, J. Fluid Mech. 53 (1972) 329–349.
[9] Pao H.-P., Kao T.W., Dynamics of establishment of selective withdrawal of a stratified fluid from a line sink. Part 1. Theory, J. Fluid Mech. 65 (1974) 657–688.
[10] Kao T.W., Pao H.-P., Wei S.N., Dynamics of establishment of selective withdrawal of a stratified fluid from a line sink. Part 2. Experiment, J. Fluid Mech. 65 (1974) 689–710.
[11] Imberger J., Thompson R., Fandry C., Selective withdrawal from a finite rectangular tank, J. Fluid Mech. 78 (1976) 489–512.
[12] Imberger J., Selective withdrawal: a review, in: 2nd Intl. Symp. on Stratified Flows, 1980, pp. 381–400.
[13] Silvester R.S., Generation of asymmetric shear fronts by selective withdrawal from a rectangular tank of linearly stratified liquid, in: 2nd Intl. Symp. on Stratified Flows, 1980, pp. 436–446.
[14] Yih C.-S., Stratified Flows, Academic Press, New York, 1980.
[15] Ingber M.S., Mitra A.K., Numerical solution of stratified flow into a sink: a criterion for selective withdrawal, J. Fluids Eng.-ASME 109 (1987) 384–388.
[16] Monismith S.G., Imberger J., Shear waves and unsteady selective withdrawal, J. Hydraul. Eng.-ASCE 114 (1988) 1134–1152.
[17] Clarke S.R., Imberger J., The effect of shear in selective withdrawal, Phys. Fluids 7 (1995) 1523–1528.
[18] Yih C.-S., Zhu S., Selective withdrawal from stratified streams, J. Aust. Math. Soc. B 38 (1996) 26–40.
[19] Ivey G.N., Blake S., Axisymmetric withdrawal and inflow in a density-stratified container, J. Fluid Mech. 161 (1985) 115–137.
[20] Kataoka T., Tsutahara M., Tanaka M., Point sink flow in a linearly stratified fluid of finite depth, Phys. Fluids 12 (2000) 2775–2786.
[21] McEwan A.D., Baines P.G., Shear fronts and an experimental stratified shear flow, J. Fluid Mech. 63 (1974) 257–272.
[22] Whitehead J.A., Selective withdrawal of a rotating stratified fluid, Dynam. Atmos. Oceans 5 (1980) 123–135.
[23] Monismith S.G., Maxworthy T., Selective withdrawal and spin up of a rotating stratified fluid, J. Fluid Mech. 199 (1989) 377–401.
[24] Mcdonald N.R., Imberger J., A line sink in a rotating stratified fluid, J. Fluid Mech. 233 (1991) 349–368.
[25] Mcdonald N.R., Imberger J., Withdrawal of a stratified fluid from a rotating channel, J. Fluid Mech. 235 (1992) 643–664.
[26] Gill A.E., Adjustment under gravity in a rotating channel, J. Fluid Mech. 77 (1976) 603–621.
[27] Lighthill J., Waves in Fluids, Cambridge University Press, Cambridge, 1978.
[28] Bender C.M., Orszag S.A., Advanced Mathematical Methods for Scientists and Engineers, McGraw-Hill, New York, 1978.
[29] Canuto C., Husseini M.Y., Quarteroni A., Zang T.A., Spectral Methods in Fluid Dynamics, Springer-Verlag, New York, 1988.